


ORIGINAL INNOVATION

Open Access



Experimental and numerical investigation into the local scour of bridge cofferdam with anti-scour ribs

Pengxin Ran¹, Kai Wei^{1*} , Bike Zhang¹, Lu Wang², Ruihua Nie² and Yongle Li¹

*Correspondence:
kaiwei@home.swjtu.edu.cn

¹ State Key Laboratory of Bridge Intelligent and Green Construction, Southwest Jiaotong University, Chengdu 610031, China

² State Key Laboratory of Hydraulics and Mountain River Engineering, College of Water Resource and Hydropower, Sichuan University, Chengdu 610065, China

Abstract

Cofferdam is widely employed in the construction of underwater bridge foundations. Its crucial attribute lies in providing a dedicated platform for construction activities and enhancing the water resistance dimensions in structural design, consequently amplifying local scour. However, previous research on local scour has seldom investigated the effect of construction facilities on the life cycle development of local scour on foundations. This gap has led to a misunderstanding of protective strategies against local scour throughout the construction period. In this paper, a scour experiment platform was implemented with a unidirectional flume. Physical model experiments were conducted to scrutinize the protective impact of anti-scour rib structures against local scour. The experimentally determined scour depth was compared to assess the performance of the anti-scour rib protection system. Oblique photogrammetry was subsequently used to capture the morphology of the equilibrium scour pit in the experiments. The associated topographical data were imported into Fluent commercial fluid software for in-depth flow field analysis. A numerical flume model was established to examine the hydraulic characteristics under two distinct topographical conditions: a smooth riverbed during the initial stage of scour and a scoured riverbed at the equilibrium stage of scour. To further determine the protective mechanism of anti-scour rib protection, the influence of anti-scour rib protection on shear stress was investigated numerically. Analyses revealed that incorporating scour protection ribs during cofferdam construction alters the flow field characteristics, hindering the downward movement of subsurface flow beneath the structure, reducing bed shear stress, and consequently mitigating scour effects. The instantaneous protective effect of scour protection ribs strengthens as the scour topography develops. The protective effectiveness of scour protection ribs was mainly influenced by rib length, spacing, and shape.

Keywords: Local scour, Experiment, Anti-scour ribs, Numerical simulation, Cofferdam construction

1 Introduction

With the development of bridges that cross rivers, straits, etc., the challenges faced in constructing bridges include technical issues and complex hydrological environments, such as issues related to local scour (David and Smith 1977, Lu et al. 2024, Wei et al.

2024). Local scour, a significant cause of water-induced damage to bridges, can result in deterioration of the bridge working environment, even leading to failure (Administration 2012). It influences the stability of infrastructure elements such as piers or embankments. Therefore, many scholars have extensively studied local scour and its prevention. Local scour refers to the formation of scour holes near bridge piers or foundations due to the obstruction of water flow by piers or foundations. In this process, eddies are generated, carrying away sediment from nearby bridge piers or foundations and resulting in the formation of scour depressions (Wang et al. 2017). Melville (Melville 1975) employed a combination of the bubble technique and quantitative measurements to study the flow field around cylindrical bridge piers and measured the shear stress distribution on the riverbed around the piers. Dargahi (Dargahi 1989, 1990) utilized the bubble technique to investigate the flow field of horseshoe vortices under turbulent conditions. Kwan and Melville (Kw An and Melville 1994) discovered that the flow structure is dominated by a primary vortex and its associated subsurface flow, considering them the main causes of scour. Abbas et al. (Abbas et al. 2020) investigated the influence of variations in the tilt angle of twin piers on local scour. They found that as the angle increased, the scour depth continuously decreased. Khaledi (Khaledi et al. 2020) studied the length and width of scour holes around a group of piles under clear-water conditions. They found that the foundation shape and the height of the supporting platform influenced the dimensions of the scour hole. Ahamed (Ahamed 1995) utilized bubble and laser techniques to investigate the detachment process of horseshoe vortices from the boundary layer. Guan and Unger (Guan et al. 2022, Unger and Hager 2007) employed Particle Image Velocimetry (PIV) to measure the velocity distribution and turbulence characteristics of horseshoe vortices at different stages of scour development. The development rate of the scour depth varies at different stages, and the factors that play a dominant role in scour also differ. Raudkivi (Raudkivi and Ettema 1983) divided the scour development process into three stages: the initiation stage, the main scour stage, and the equilibrium scour stage. Chiew (Chiew and Yee-Meng 1992) categorized bridge foundation scour protection measures into active and passive protection measures. Kumar et al. (Kumar et al. 1999) studied the protective effects of different collar installation heights and collar sizes on scour prevention. Moncada-M (Moncada-M et al. 2009) reported that the scour depth decreases with increasing pier opening length. Under the considered flow conditions, the combination of pier openings and collars can eliminate scour efficiently. Zarrati (Zarrati et al. 2004) conducted experimental studies on the application of collars to protect against scour around rectangular bridge piers. They found that as the inclination angle of the pier increased, the protective efficacy of the collar decreased. The literature has focused primarily on local scour around bridge pier foundations after construction, with limited research on local scour during construction. Wei (Wei et al. 2022) conducted experiments and numerical simulations to study the protective effect of a skirted caisson on the depth of local scour. This research aimed to elucidate the development patterns of the maximum scour depth and the scour mechanism. Xiang (Xiang et al. 2020) investigated the influence of the suspended sinking time of caissons on local scour. Luo (Luo et al. 2022) conducted experiments to study the protective effectiveness of horn-shaped collars against local scour. Abdelmoaty (Abdelmoaty and Zayed 2021) studied the influence of side flow jets at different angles on the downstream local scour

depth and energy dissipation. Qiu (Qiu et al. 2023) researched the impact of local scour depth, model dimensions, and model shape on hydraulic forces. Wang (Wang et al. 2019) conducted experiments to study the influence of key parameters of anti-scour collars on local scour protection. Melville (Melville and Hadfield 1999) reported that the protective efficiency of sacrificial piles depends on factors such as their arrangement and the angle of water flow. Many researchers have also studied passive protection measures, such as riprap protection and expanding foundation protection (Chiew 1997, Lauchlan and Melville 2001, Parola et al. 1996). However, deep-water foundations require the creation of a construction environment through cofferdams during construction. Cofferdams, in turn, increase the watertight area considered in foundation design, intensifying the development of local scour and posing a risk to the structural integrity of bridges.

In summary, this paper conducts physical model experiments on cofferdams as the research subject, focusing on rib-type scour protection against local scour. The effectiveness of rib-type scour protection is explored by comparing the experimentally measured scour depths. In addition, oblique photogrammetry was used to measure the morphology of the experimental scour holes. The scanned topography is then imported into the commercial fluid software Fluent for flow field analysis. A numerical model of the flume is established to analyze the hydrodynamic characteristics of different key parameters of the scour protection ribs. This research investigated the variations in bed shear stress and the Z-direction flow velocity at the riverbed bottom, revealing the mechanisms of rib-type scour protection. This study aimed to provide insights into local scour protection during the construction phase of cofferdams around underwater bridge piers.

2 Experimental study

2.1 Experimental facilities

The experiment uses a unidirectional circulating water flume with a length of 8 m, a width of 0.4 m, and a height of 0.6 m. The upstream inlet is equipped with a rectifying grating and an inlet. The downstream outlet is connected to a water tank and a pump. In the rear section of the flume, there is a scour test pit with a length of 1 m and a height of 0.13 m, which is designed for filling with sediment for scour experiments. The experimental setup is illustrated in Fig. 1.

2.2 Velocity measurements

The experiment employed a Doppler velocimeter for velocity measurement with a sampling frequency of 200 Hz. The probe of the Doppler velocimeter was placed 0.02 m below the water surface to measure the velocity variation curve. As shown in Fig. 2(a), there was no significant change in velocity within 10 seconds. Therefore, the average velocity at this height was selected for analysis.

By placing the probe of the experimental flume below the water surface and moving it downward at intervals of 0.01 m, the distribution of the cross-sectional flow velocity along the height of the flume was obtained, as shown in Fig. 2(b). The figure shows that the flow velocity is generally stable within 0.04 m from the water surface. Therefore, the

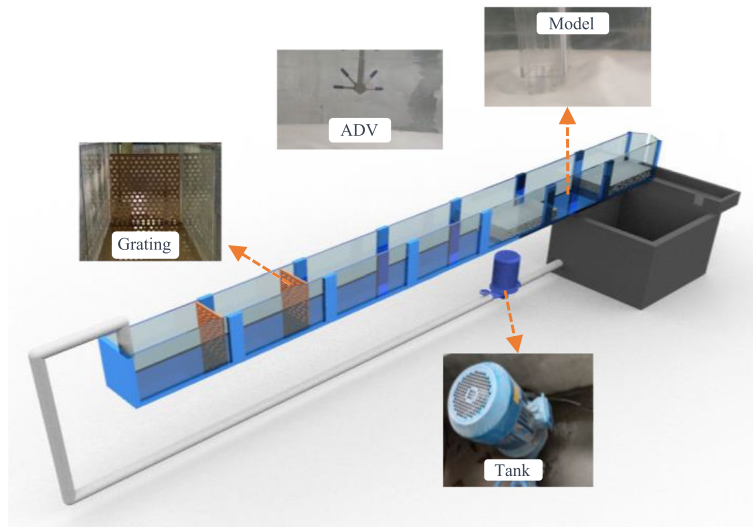


Fig. 1 Experimental flume system

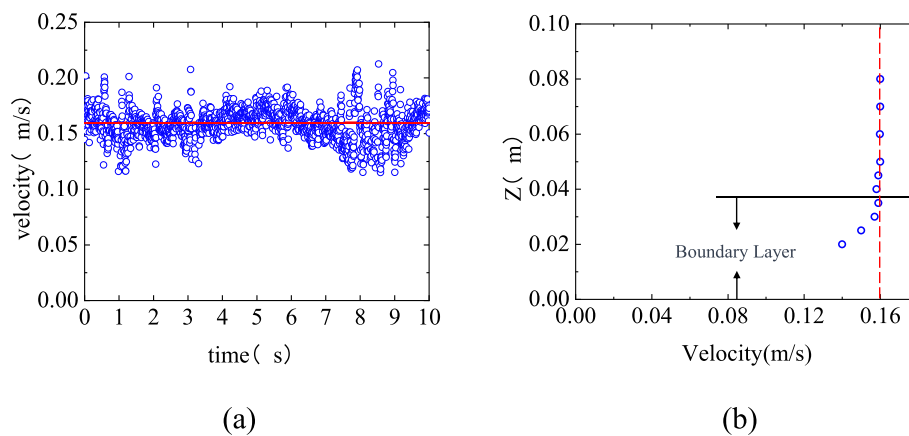


Fig. 2 Flow velocity measurements: (a) velocity at 0.02 m; and (b) velocity profile

flow conditions for this experiment included a water depth of 0.1 m and a flow velocity of 0.16 m/s.

2.3 Sediment conditions in the experiment

The gradation of the experimental sediment was measured using a medium-sized sediment shaking sieve, and the particle size distribution curve of the model sand was obtained, as shown in Fig. 3. The density of the quartz sand particles was 2.65 g/cm³, and the particles had a diameter of 0.2 mm. The sediment initiation flow velocity was calculated using the sediment initiation flow velocity calculation formula proposed by Soulsby (Soulsby 1997):

$$\theta_{cr} = \frac{0.3}{1 + 1.2D_*} + 0.055[1 - \exp(-0.02D_*)] \tag{1}$$

$$D_* = [g(s - 1)/\nu^2]^{1/3}d_{50} \tag{2}$$

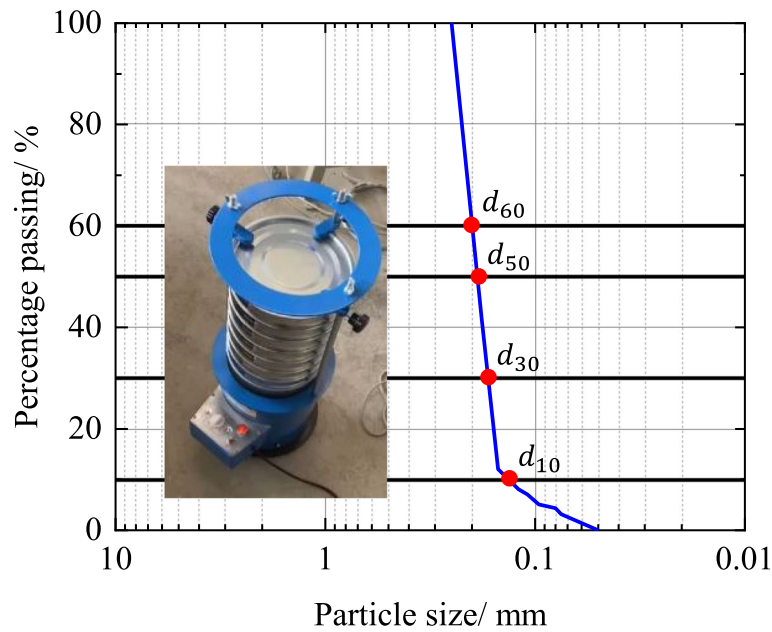


Fig. 3 Gradation curve of model sand grain sizes

$$\theta_s = \frac{\tau_s}{\rho g(s-1)d_{50}} = \frac{U_{fs}^2}{g(s-1)d_{50}} \tag{3}$$

$$\tau_s = \rho C_D \bar{U}^2 \tag{4}$$

$$C_D = \{\kappa / [\ln(z_{0s}/h) + 1]\}^2 \tag{5}$$

where θ_{cr} is critical Shields number, D_* is nondimensional particle diameter, g is gravity acceleration (-9.8 m/s^2), s is sediment density (2.65), ν is the dynamic viscosity of water ($10^{-6} \text{ m}^2/\text{s}$), d_{50} is median particle size (0.2 mm), θ_s is bed surface friction Shields number, τ_s is shear stress of flow, U_{fs} is frictional flow velocity, \bar{U} is average flow velocity (0.16 m/s), h is depth of water (0.1 m), κ is Karman constant (0.4), z_{0s} is the bed roughness ($d_{50}/12$)

The simultaneous solution of Eqs. 1, 2, 3, 4 and 5 enables a comparison between the critical Shields number and the bed surface Shields number, aiding in determining whether the flow can meet the conditions for sediment initiation.

The calculations revealed that the critical vertical mean flow velocity for sediment initiation was approximately 0.25 m/s. As shown in Fig. 2, the experimental mean flow velocity was approximately 0.16 m/s. Therefore, the scouring mode in this study was consistent with clear water scouring.

2.4 Determination of the scour testing duration

The scouring modes are primarily categorized as clear-water scour or live-bed scour. Due to its relatively low flow velocity, clear-water scour requires a longer development time to reach equilibrium than live-bed scour (Raudkivi and Ettema 1983). Therefore,

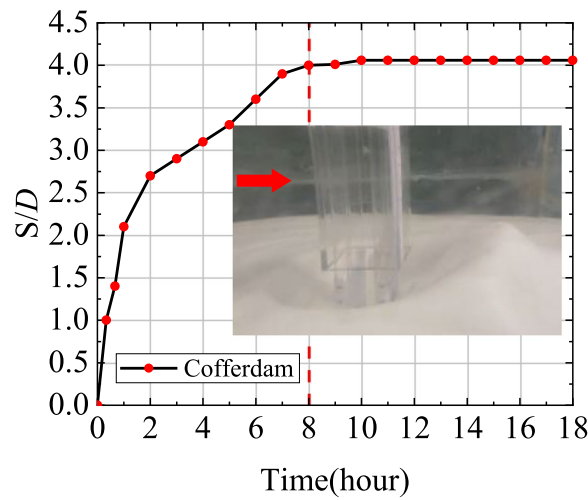


Fig. 4 The maximum scour depth of the cofferdam

Table 1 Parameter settings of the experimental conditions

Test	Foundation	Cofferdam	Anti-scour rib
1	Pile group	-	-
2	Pile group	√	-
3	Pile group	√	√

determining when the experiment reaches scour equilibrium is crucial. In this study, we initially conducted an 18-hour cofferdam construction scour test, and the time–depth curve for the maximum scour depth is presented in Fig. 4. The figure shows that the maximum scour depth exhibited no significant changes after 8 hours of experimental development, indicating that scour equilibrium was reached. A subsequent scour test duration of 12 hours was chosen to ensure that the experiment reached equilibrium. It is worth emphasizing that all scour depths mentioned in the text refer to nondimensionalized scour depth S/D .

2.5 Experimental cases

Three scour test conditions were used to investigate the impact of cofferdam construction during the construction phase on local scour and the effectiveness of scour protection by anti-scour ribs, as shown in Table 1. The model, made of acrylic material, consisted of a group of piles with a diameter of 1 cm. Four piles were evenly spaced at intervals of 2.5 cm and were surrounded by a thin-walled cofferdam with dimensions of 4 cm in length and width, as illustrated in Fig. 5. B refers to the width of the watertight barrier at the outer boundary of the cofferdam. D refers to the diameter of the individual piles in the pile group. The anti-scour ribs had a length (L) and width (W) of 5 mm, corresponding to $0.5 D$, respectively, relative to the cofferdam and individual pile dimensions. The particles were uniformly distributed in the vertical direction with a spacing of 2 cm, as shown in Fig. 6.

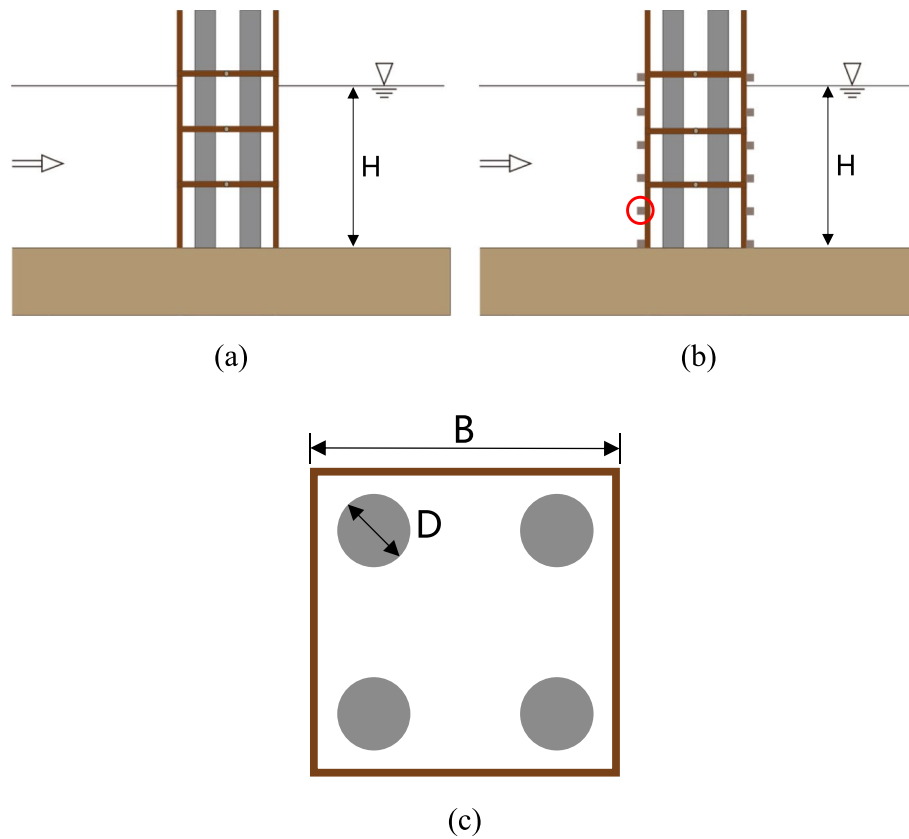


Fig. 5 Diagram of the cofferdam model: (a) cofferdam; (b) anti-scour rib; and (c) top view of the experimental model

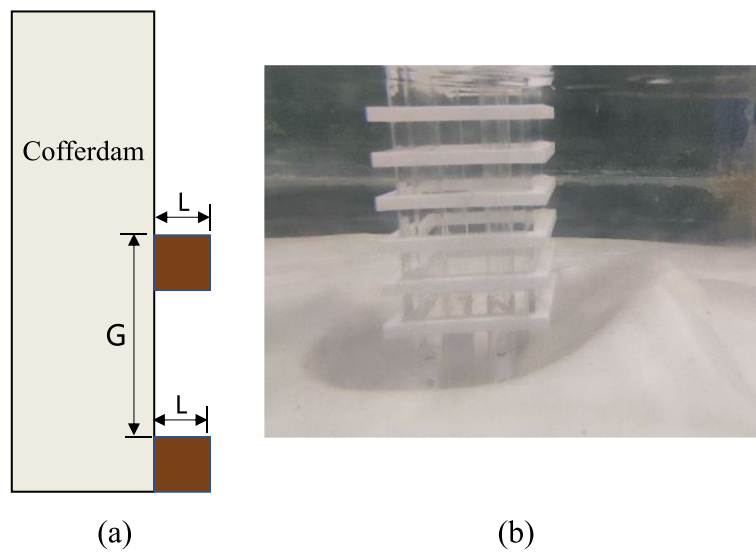


Fig. 6 Local diagram of the anti-scour rib: (a) parameters of the anti-scour ribs; and (b) experimental process

2.6 Measurement of the scoured terrain using oblique photogrammetry

During the experimental process, underwater high-definition cameras were used to collect scour depth data at the measurement points. In the first hour of the experiment, data were collected every 20 minutes, and after one hour, the data collection intervals were extended to every 60 minutes.

After the end of the experiment, the flume was drained, and the system was left undisturbed for one day. Subsequently, oblique photogrammetry was used to scan the morphology of the scour pit. An oblique photogrammetry platform was established using commercial software (ContextCapture). High-definition cameras capture texture information by photographing scour pits at various angles. Finally, aerial triangulation calculations were performed to acquire precise textural coordinates, creating a three-dimensional model of the scour pit, as shown in Fig. 7.

3 Numerical simulation

3.1 Basic principles

Using the RNAS equation of the RNG $k - \epsilon$ turbulence model as the governing equation for incompressible viscous fluid:

$$\frac{\partial \rho}{\partial t} + \frac{\partial}{\partial x_i}(\rho u_i) = 0 \tag{6}$$

$$\frac{\partial}{\partial t}(\rho u_i) + \frac{\partial}{\partial x_j}(\rho u_i u_j) = -\frac{\partial p}{\partial x_i} + \frac{\partial}{\partial x_j}[\mu(\frac{\partial u_i}{\partial x_j} + \frac{\partial u_j}{\partial x_i} - \frac{2}{3}\delta_{ij}\frac{\partial u_l}{\partial x_l})] + \frac{\partial}{\partial x_j}(-\rho \overline{u_i' u_j'}) \tag{7}$$

where ρ is the density of water, t is time, x_i and x_j are coordinate position, u_i, u_j, u_l are velocity component, p is pressure, δ_{ij} is the Kronecker function, u_i is mean velocity, u_l is fluctuating velocity.

The RNG $k - \epsilon$ turbulence equation is as follows:

$$\frac{\partial}{\partial t}(\rho k) + \frac{\partial}{\partial x_i}(\rho k u_i) = \frac{\partial}{\partial x_j}(\alpha_k \mu_{eff} \frac{\partial k}{\partial x_j}) + G_k + G_b - \rho \epsilon + S_k \tag{8}$$

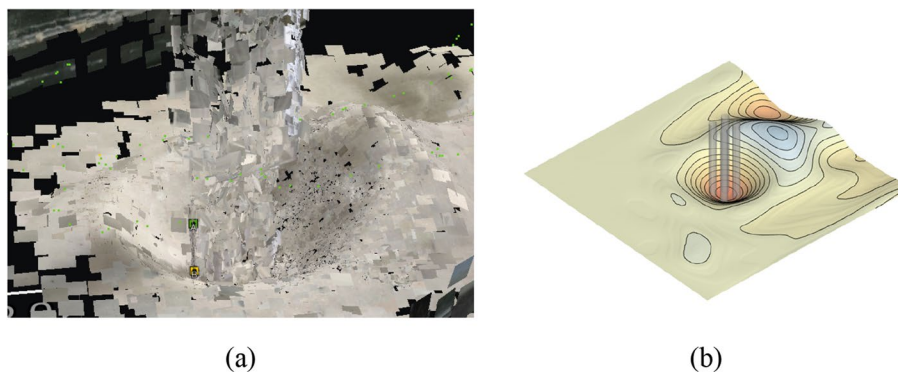


Fig. 7 Oblique photogrammetry: (a) image information collection; and (b) schematic of topography scanning

$$\frac{\partial}{\partial t}(\rho \varepsilon) + \frac{\partial}{\partial x_i}(\rho \varepsilon u_i) = \frac{\partial}{\partial x_j}(\alpha_\varepsilon \mu_{eff} \frac{\partial \varepsilon}{\partial x_j}) + C_{1\varepsilon} \frac{\varepsilon}{k} (G_k + C_{3\varepsilon} G_b) - C_{2\varepsilon} \rho \frac{\varepsilon^2}{k} - R_\varepsilon + S_\varepsilon \tag{9}$$

where k is turbulent kinetic energy, ε is dissipation rating, $\alpha_k, \alpha_\varepsilon$ are inverse effective Prandtl number, μ_{eff} is effective viscosity, G_k is the turbulent energy generated by the mean velocity gradient ($G_k = \mu_t (\partial u / \partial z)^2$), G_b is the turbulent kinetic energy generated by buoyancy, $C_{1\varepsilon}, C_{2\varepsilon}, C_{3\varepsilon}$ is turbulence model constant, $R_\varepsilon = \frac{C_{\mu} \rho \eta^3 (1 - \eta / \eta_0) \varepsilon^2}{1 + \beta \eta^3} \frac{\varepsilon^2}{k}$, $C_\mu = 0.0845, \eta = S_k / \varepsilon, \eta_0 = 4.38, \beta = 0.012$.

The standard wall function is used to calculate the shear near the wall:

$$\frac{\partial \bar{\rho} \tilde{u}}{\partial x} + \frac{\partial \bar{\rho} \tilde{v}}{\partial y} = 0 \tag{10}$$

$$\frac{\partial}{\partial y} \{ \tau_{xy} - \bar{\rho} u'' v'' \} = 0 \tag{11}$$

$$\frac{\partial}{\partial y} \{ \tau_{xy} u + k \frac{\partial T}{\partial y} \} = 0 \tag{12}$$

$$\mu \frac{\partial u}{\partial y} = (\mu \frac{\partial u}{\partial y})_{y=0} = \tau_w \tag{13}$$

where the x direction indicates the flow parallel to the wall, the y direction indicates the normal direction of the wall, and τ_w is wall shear.

3.2 Numerical flume

This study used the commercial software Fluent v211 to conduct detailed simulations of the flow field under local scour topography and initial topography, exploring the scour characteristics and protective mechanisms. The numerical flume had the same width and depth as the experimental conditions, with a width 10 times B to meet the blockage ratio requirements. To ensure that the flow field developed to a steady state, the total length of the flume was set to 2 m, which is 50 times the width of the cofferdam (B). The structural center was 35 B from the inlet and 15 B from the outlet, as shown in Fig. 8. In the flow development section, the bottom of the flume was flat, and the three-dimensional scour topography obtained by oblique photogrammetry was imported around the structure. The inlet was set as a velocity boundary, the

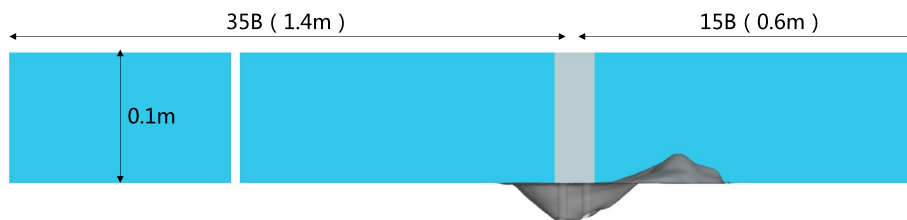
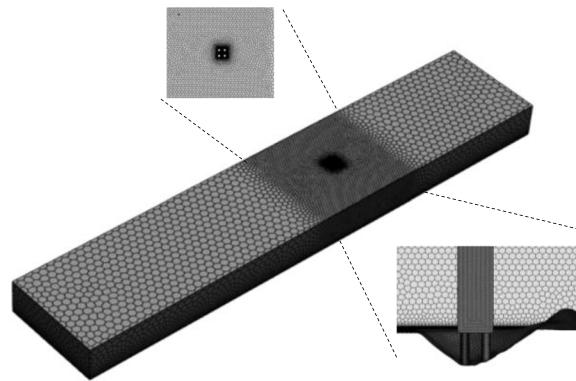


Fig. 8 Numerical flume with scoured scour hole terrain

Table 2 Parameter settings of the numerical simulation

Test	Anti-scour rib	L	G	Shapes
#1	-	-	-	-
#2	√	0.075B	0.5B	square
#3		0.125B		
#4		0.175B		
#5	√	0.125B	0.25B	square
#6			0.75B	
#7	√	0.125B	0.5B	L-shaped

**Fig. 9** Mesh of the 3D numerical flume

outlet was set as a pressure outlet boundary, the bottom and two sidewalls were set as wall boundaries according to the experimental conditions, and the top was set as an atmospheric pressure boundary. The roughness height of the bottom wall boundary was taken as the sediment grain size of 0.2 mm. The model mainly studies the protective mechanisms and the influence of critical parameters of anti-scour ribs on the initial bed shear stress and Z-directional velocity of the bed surface, as shown in Table 2.

3.3 Mesh partitioning and verification

The mesh partitioning of the numerical tank model is illustrated in Fig. 9. Local refinement is applied around the structure and topography areas by utilizing an unstructured mesh for the entire model. The dimensions of the structure surface, topography surface, and overall scour terrain are 0.001 m, 0.005 m, and 0.01 m, respectively, with the maximum size of the entire domain being 0.032 m. Subsequently, an adaptive mesh encompassing hexahedra and polyhedra is generated based on the surface mesh, resulting in a total mesh count of approximately 700,000. Replicating the flow conditions of Test Case 1, with a velocity of 0.16 m/s and a water depth of 0.1 m in the numerical tank, the model is compared to the experimentally measured flow velocity at the midline of the tank, 5 B distances in front of the structure. The model exhibits good agreement, meeting the requirements of flow field simulation, as illustrated in Fig. 10 (Roulund et al. 2005).

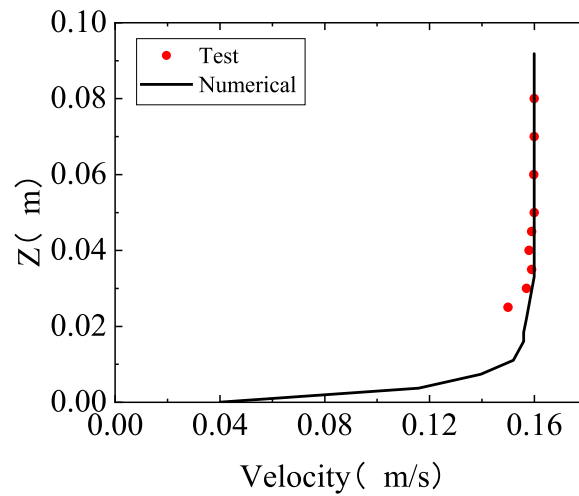


Fig. 10 Comparison of the measured and simulated flow velocities

4 Results and discussion

This section summarizes the effectiveness of local scour protection and scour characteristics associated with cofferdam construction under identical hydraulic conditions considering the presence of scour protection ribs. Drawing insights from the results obtained through experimental topography and numerical simulations of the flow field, the impact of key parameters related to scour protection ribs on bed shear stress and Z-direction velocity is examined.

4.1 The effect of a cofferdam on local scour

This article first investigates the local scour characteristics of a group pile foundation under the influence of cofferdam construction. The time–depth curves of the maximum scour depth for two conditions, one with the group pile foundation and the other with the cofferdam resting directly on the bed, are shown in Fig. 11. It can be observed from

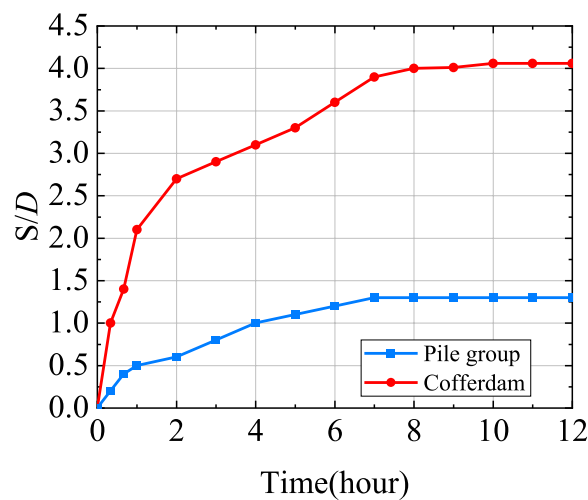


Fig. 11 Scour depth of cofferdam construction

the figure that under the same flow conditions, the maximum scour depth for the group pile foundation is significantly smaller than that for the cofferdam bed. This is because the original individual pile diameter of the group pile foundation was 1 cm, and after the arrangement, the water-blocking width was 2 cm. After the cofferdam bed construction, the water-blocking width above the riverbed surface doubled to 4 cm. With the increase in water-blocking width, the structure hindered the formation of horseshoe vortices and intensified the downward flow, exacerbating the excavation of sediment around the structure. As a result, the maximum scour depth increased from 1.3 cm to 4.06 cm.

A schematic diagram of the terrain along the X-Z section of the maximum scour depth is shown in Fig. 12. As observed from the figure, cofferdam construction significantly influences the local scour around the group pile foundation, enlarging the depth and extent of the scour hole. The sediment accumulation height behind the structure increased from 1.2 cm to 3 cm, but the location of the maximum scour depth remained in front of the upstream side of the pile foundation.

4.2 The effect of Anti-scour ribs on local scour

4.2.1 Characteristics of local scours

The scour depth–time curves for the outer surface of the cofferdam with scour protection ribs are presented in Fig. 13. Close examination of the figure reveals that under identical flow conditions, there is no significant difference in the maximum scour depth between the cofferdam without protection ribs and the cofferdam with protection ribs during the initial 4 hours of the scour test. The scour depth rapidly develops in the early stages, ranging from 0 to 1 hour. The period spanning from 1 to 8 hours corresponds to the primary scour stage during cofferdam construction without protection and is characterized by a gradual increase in the scour depth and a diminishing rate of scour depth development. Subsequently, the equilibrium scour stage is reached, and the maximum scour depth is recorded at 4.06 cm. In the scenario with scour protection ribs, a noticeable distinction emerges after 4 hours of the scour test in comparison to the unprotected condition. The scour development stage concludes earlier, reaching the equilibrium scour stage at 6 hours, with a maximum scour depth of approximately 3.28 cm, representing a reduction of approximately 20% compared to the unprotected condition.

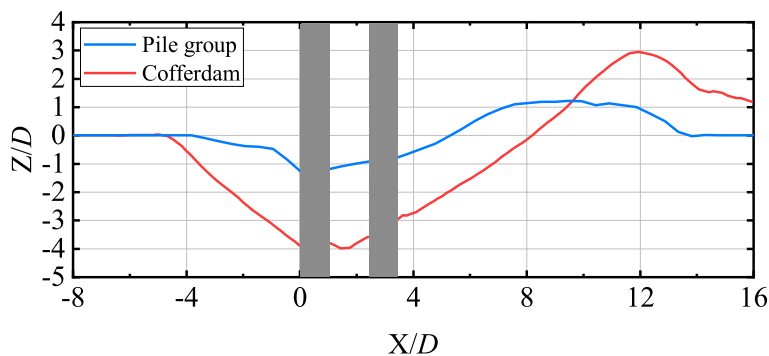


Fig. 12 The X-Z section of the cofferdam construction

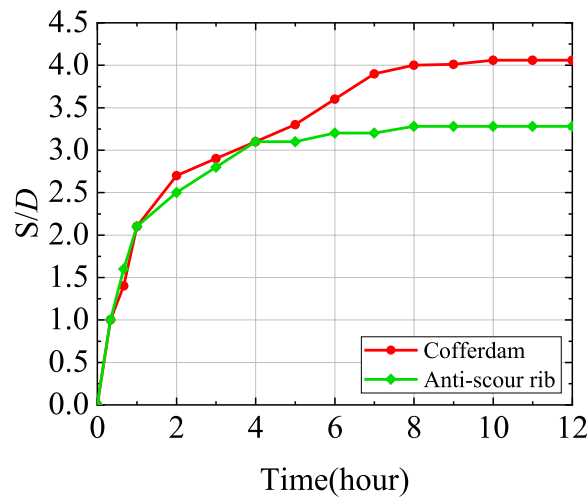


Fig. 13 Scour depth of the Anti-scour rib

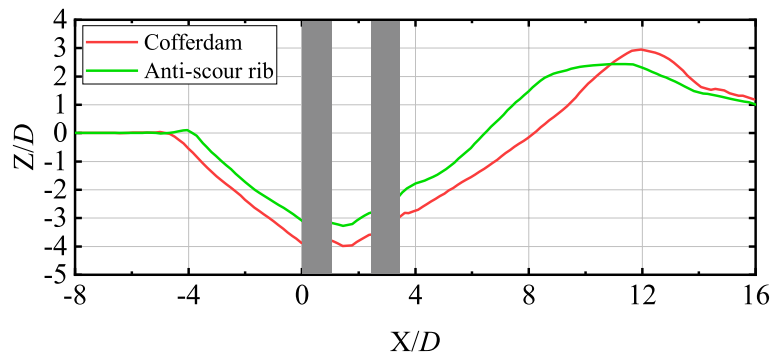


Fig. 14 The X-Z section of the anti-scour rib

A schematic diagram of the X-Z cross section of the scour pit is shown in Fig. 14. The figure shows that in the equilibrium scour state, the scour protection ribs reduce the overall extent of the equilibrium scour pit. In the unprotected condition, the front end of the scour pit is approximately 5 cm from the foundation’s leading edge, while in the scenario with scour protection ribs, it is approximately 4 cm. The heights of sediment deposition at the rear were 3 cm and 2.5 cm, respectively.

4.2.2 Characteristics of the hydrodynamics

The influence of scour protection ribs on the streamlines around the structure under scour terrain conditions is depicted in Fig. 15. The figure shows that under unprotected conditions, the structure impedes the motion of water, reducing the flow velocity behind the structure and generating a downflow along the structure surface and horseshoe vortices near the scour pit. These combined effects transport sediment. The scour protection ribs exhibit a positive protective effect at this point, hindering the downflow along the structure surface and creating vortices near the scour protection ribs. This disrupts the energy of the downflow, reducing its erosive capacity for sediment.

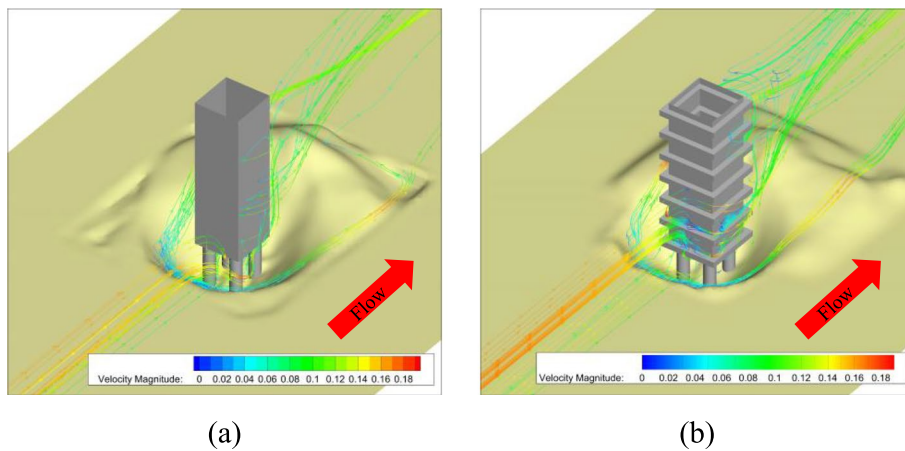


Fig. 15 Flow streamlines around the anti-scour rib: (a) Cofferdam; and (b) Anti-scour rib

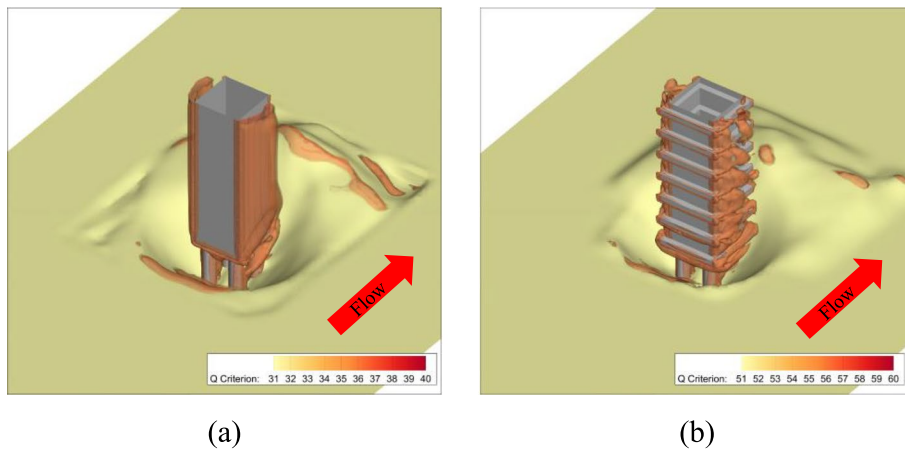


Fig. 16 Vorticity around the anti-scour rib: (a) Cofferdam; and (b) Anti-scour rib

A vorticity map of the flow field near the structure under scour terrain conditions is shown in Fig. 16. From the figure, it is evident that in the unprotected condition, many vortices appear near the corners of the square cofferdam and on the downstream side. As the terrain reaches an equilibrium state and no longer changes, the horseshoe vortex intensity on the upstream side of the scour pit decreases, leading to less surface sediment erosion. The presence of scour protection ribs considerably impacts the entire vortex field. By impeding the movement of the downflow, the scour protection ribs cause a minimal amount of vortices to appear above and below the upstream face of the scour protection ribs. This disturbance extends to the vortex field near the corners of the cofferdam, resulting in widespread disruption of the vortices. Overall, the vortex intensity decreases, contributing to a protective effect against scour.

Figure 17(a) and (b) depict the initial bed shear stress calculated through numerical simulation. From the figure, it can be observed that in the initial terrain state, the obstructions of the cofferdam without protection ribs and the cofferdam with protection ribs on water flow are similar, with comparable maximum values of bed shear stress,

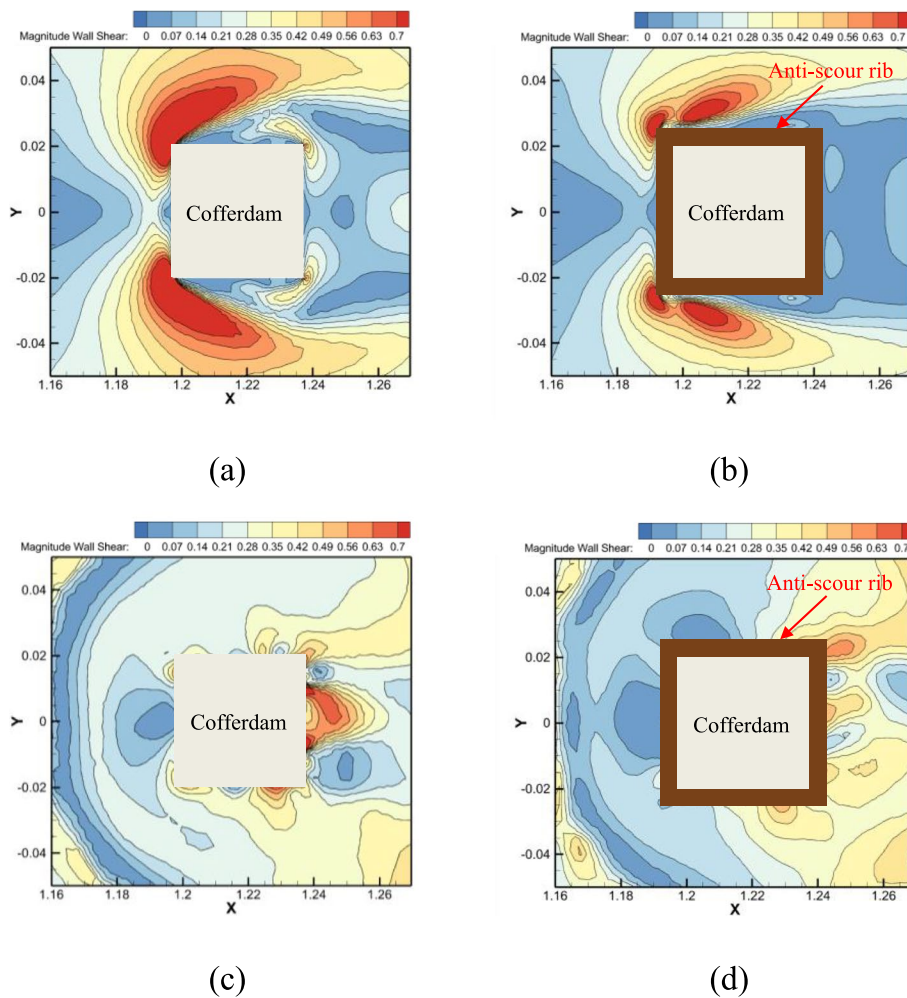


Fig. 17 The shear stress of different scour terrains: **(a)** Cofferdam with initial terrain; **(b)** Anti-scour rib with initial terrain; **(c)** Cofferdam with scoured terrain; and **(d)** Anti-scour rib with scoured terrain

indicating similar excavation intensities of sediment. However, due to the disturbance caused by the scour protection ribs on the flow field, there are differences in the locations where the maximum bed shear stress occurs. In the unprotected condition, damage occurs near the corners on both sides of the upstream face of the square cofferdam, forming a continuous region. In the protected condition with scour protection ribs, irregular vortices are generated near the corners of the cofferdam due to the influence of the protection ribs, causing interruptions in the region of maximum bed shear stress behind the corners. Figure 17(c) and (d) illustrate the bed shear stress of the equilibrium scour terrain. As the scour pit reaches an equilibrium state, with the expansion of the sediment pit, the distance between the downflow and the horseshoe vortex reaching the riverbed surface remains constant. The scour pit no longer changes, and the bed shear stress is significantly lower than that in the initial flat terrain moment.

Figure 18 displays the maximum bed shear stress under the four conditions. In the initial stages of the experiment on flat terrain, scour protection ribs had a relatively weak protective effect on the bed shear stress. The unprotected condition exhibited

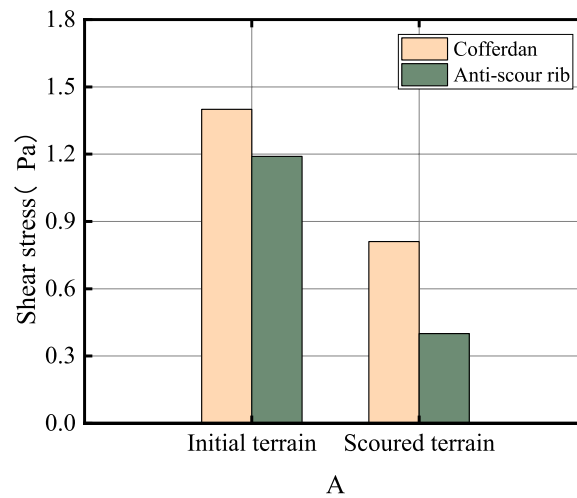


Fig. 18 The maximum shear stress of different scour terrains

a maximum bed shear stress of approximately 1.4 Pa, while the scour protection ribs reduced the shear stress to approximately 1.18 Pa, indicating a reduction of approximately 15%. Consequently, the maximum scour depth development rates in Fig. 13 are similar. In the equilibrium scour terrain flow field during the experimental stage, the maximum bed shear stress decreases as the scour terrain stabilizes. In the unprotected condition, the maximum bed shear stress is approximately 0.8 Pa, whereas under the influence of scour protection ribs, it is approximately 0.4 Pa, representing a reduction of approximately 50.6%. The development rate of the maximum scour depth gradually diminishes compared to that of the unprotected condition. This phenomenon is attributed to the initial experimental phase, in which the sediment surface is close to the cofferdam bottom, and the cofferdam hinders the erosive effects of the downflow and horseshoe vortex on the sediment. The scour protection ribs, which are smaller than the cofferdam, initially have a limited interception effect on the downflow and horseshoe vortex. As the scour depth increases, the influence distance of the downflow and horseshoe vortex on the sediment expands, reducing their intensity. Consequently, the protective impact of scour protection ribs intensifies, resulting in a more significant reduction in bed shear stress and effective scour protection.

4.3 The effect of anti-scour ribs on hydrodynamics

Melville (1975) measured the shear stress distribution around bridge piers and found a strong correlation between sediment bed shear stress and the ultimate equilibrium scour depth. When there are many structural design parameters but the experimental time is limited, the shear stress can be used to evaluate the local scour qualitatively instead of the equilibrium scour depth. In this section, the effect of rib design parameters on the scour are investigated using the simulated flow field and sediment bed shear stress.

4.3.1 The effect of the length

Figure 19 shows the flow field around the cofferdam and the Z-direction flow velocity in the X-Z cross section at the initial moment under different scour protection rib lengths.

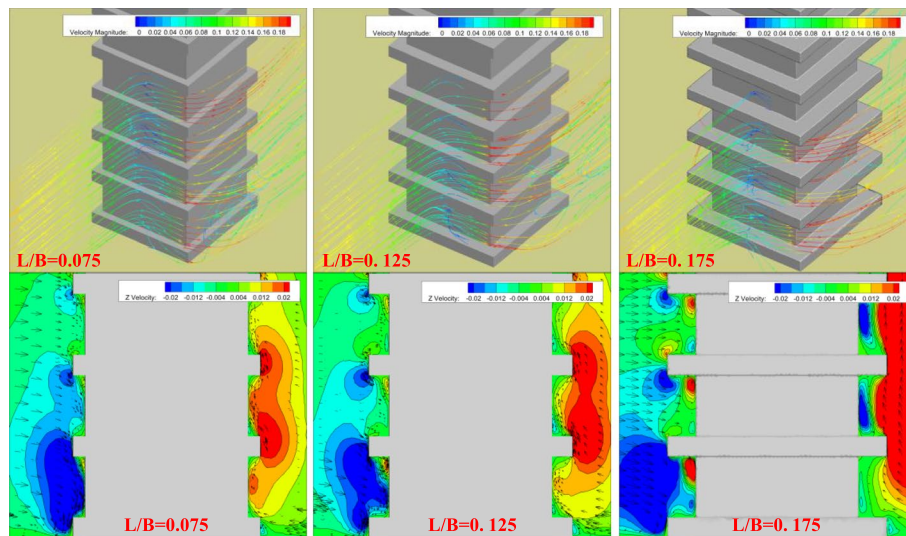


Fig. 19 Flow streamlines for different L/B ratios

The Z-direction flow velocity on the riverbed surface directly affects the occurrence of scour. Under unchanged conditions, as the length of the scour protection ribs increases, their hindrance to the downflow on the structure surface strengthens, leading to significant variations in the Z-direction flow velocity between the scour protection ribs. Taking $L/B=0.125$ as the control group, the pattern of the maximum Z-direction flow velocity at the riverbed bottom in front of the structure is as follows: $L/B=0.075 > L/B=0.125 > L/B=0.175$. When L/B increases from 0.075 to 0.125, the maximum velocity decreases by approximately 24.8%, and further increasing to 0.175 results in a reduction of approximately 7%.

Figure 20 compares the distributions of bed shear stress under different lengths of scour protection ribs. As observed in the figure, the bed shear stress on the riverbed surface decreases due to the hindrance effect of scour protection ribs, and the influence range of bed shear stress is reduced. The numerical variation pattern of the maximum shear stress is as follows: $L/B=0.075 > L/B=0.125 > L/B=0.175$. When L/B increases from 0.075 to 0.125, the maximum shear stress decreases by approximately 32.7%. Further increasing to 0.175 results in a reduction in the shear stress of approximately 10%. The overall variation pattern aligns with the pattern of changes in the Z-direction flow velocity at the riverbed bottom. The protective effect significantly improved when the concentration increased from 0.075 to 0.125, and the subsequent increase to 0.175 cm⁻¹ resulted in a relatively smaller enhancement in the protective effect, as shown in the Fig. 21.

4.3.2 The effect of the gap

Figure 22 shows the flow field around the cofferdam at the initial moment under the influence of different spacings of the scour protection ribs, along with the Z-direction flow velocity in the X-Z cross section. Under unchanged conditions, the protective effect of scour protection ribs gradually diminishes with increasing rib spacing. Using $G/B=0.5$ as the control group, the pattern of maximum Z-direction flow velocity changes

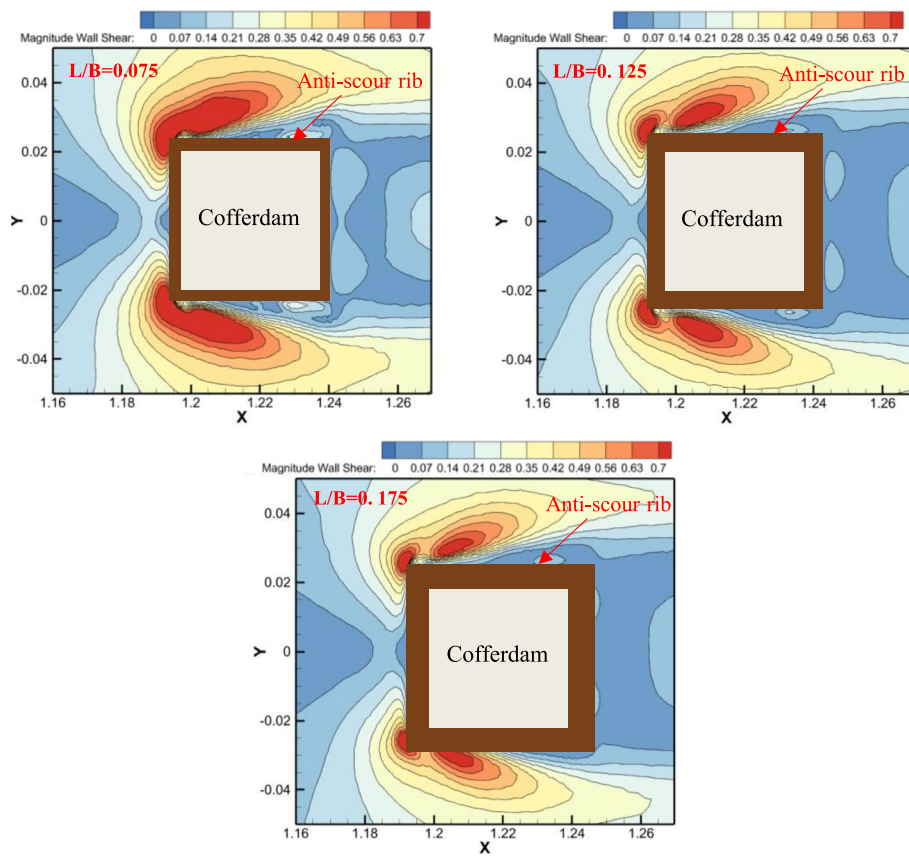


Fig. 20 The shear stress for different L/B ratios

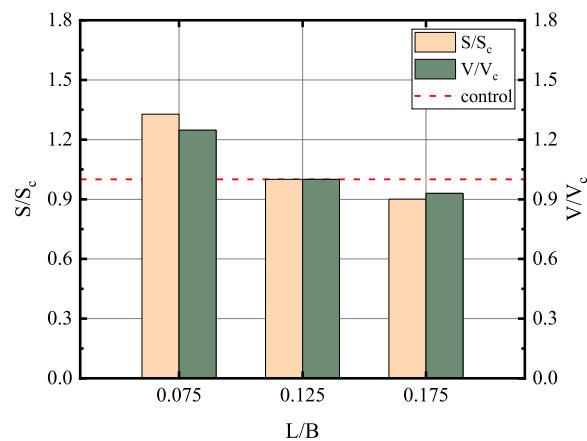


Fig. 21 The maximum shear stress and Z velocity for different L/B ratios

at the riverbed bottom in front of the structure is as follows: $G/B=0.25 < G/B=0.5 < G/B=0.75$. As G/B increases from 0.25 to 0.5, the maximum velocity remains nearly constant and slightly decreases by 8%. With a further increase to 0.75, the protective effect of the scour protection ribs weakens, and the Z-direction flow velocity increases significantly, by approximately 25%.

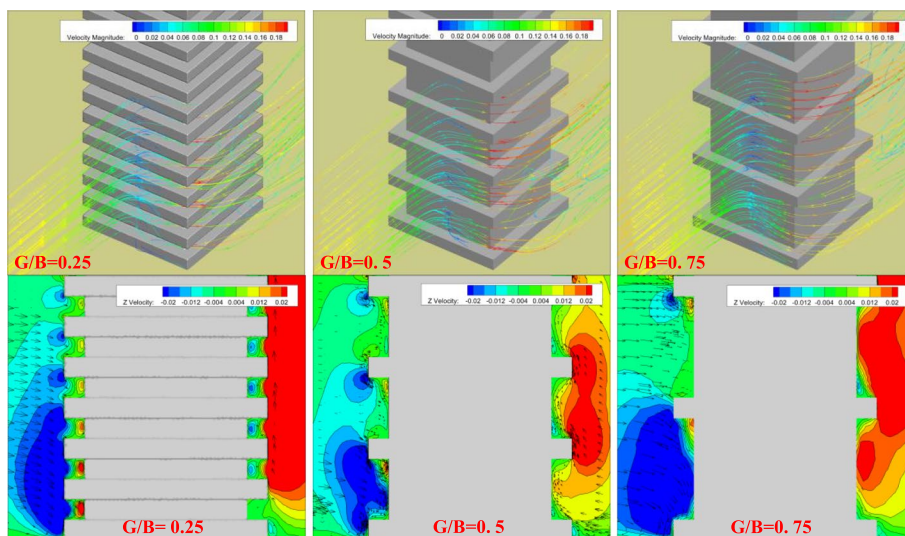


Fig. 22 Flow streamlines for different G/B ratios

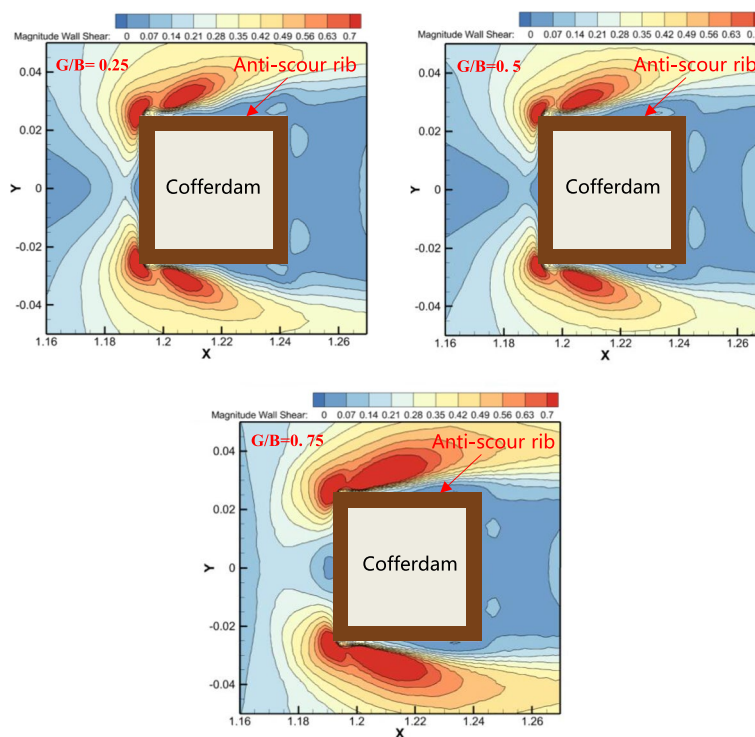


Fig. 23 The shear stress for different G/B ratios

Figure 23 compares the distributions of bed shear stress under different spacings of scour protection ribs. The figure shows that when the scour protection ribs are densely arranged, their protective effect does not continue to increase. However, when the spacing between the scour protection ribs increases, a noticeable decrease in the protective effect occurs. The numerical variation pattern of the maximum shear stress is as follows: $G/B=0.25 < G/B=0.5 < G/B=0.75$. As G/B increases from 0.25 to 0.5, the maximum

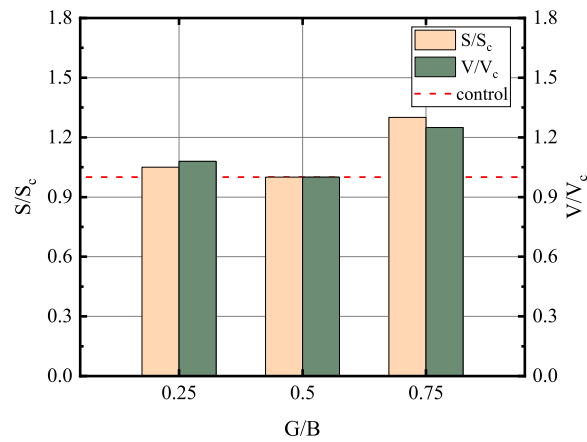


Fig. 24 The maximum shear stress and Z velocity for different G/B ratios

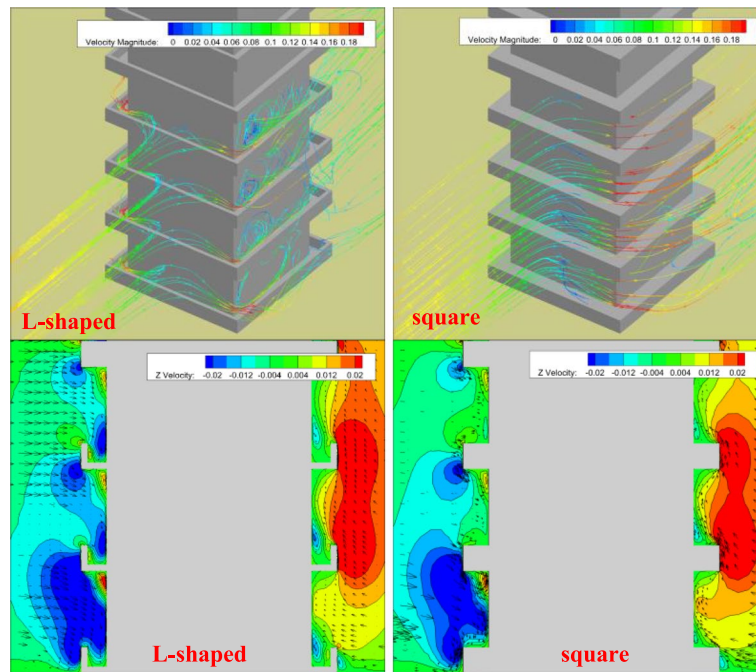


Fig. 25 Flow streamlines of different shapes

shear stress slightly decreases by 5%, and with a further increase to 0.75, it increases by approximately 30%, as shown in the Fig. 24.

4.3.3 The effect of shape

Figure 25 shows the flow field around the cofferdam at the initial moment under the influence of different shapes of scour protection ribs and different Z-directional flow velocities in the X-Z cross section. With other conditions held constant, the protective effect of the L-shaped cross section is noticeably superior to that of the square-shaped cross section. Using the square-shaped cross section as the control group, the variation pattern of the Z-directional flow velocity at the riverbed bottom in front of the structure

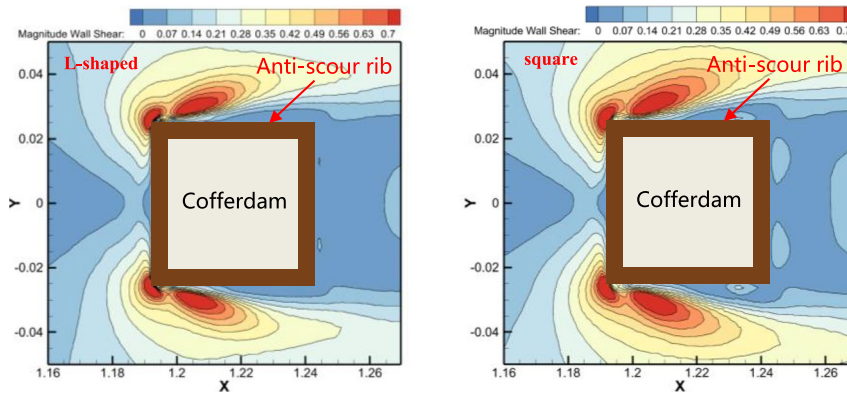


Fig. 26 Shear stress for the different shapes

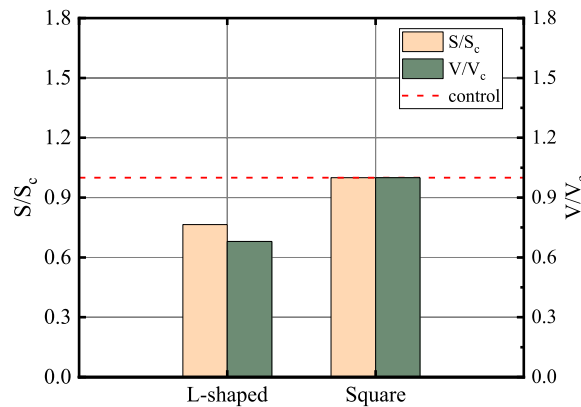


Fig. 27 Maximum shear stress and Z velocity for the different shapes

is as follows: L-shaped < square-shaped. Compared to that of the square-shaped scour protection ribs, the maximum flow velocity of the L-shaped ribs decreases by approximately 32%.

Figure 26 compares the distributions of bed shear stress under different shapes of scour protection ribs. The figure shows that the protective effect of the L-shaped scour protection ribs on the bed shear stress is significantly superior to that of the square-shaped ribs, with a reduction of approximately 24.6% in the maximum bed shear stress, as shown in the Fig. 27.

5 Conclusions

This study investigated the influence of scour protection ribs and their critical parameters on the local scour characteristics of bridge pier foundations based on both flume experiments and numerical simulations. The protective mechanism of anti-scour ribs, which helps alleviate local scour during the construction phase of bridges under unidirectional water flow, was revealed.

- (1) During cofferdam construction, the inclusion of scour protection ribs reduces the equilibrium scour depth. In the early stages of the experiment, the maximum scour depth development rate with scour protection ribs was similar to that of the unpro-

tected condition. However, in the later stages, the protective effect of the scour protection ribs strengthens, reducing the scour development rate. Under identical experimental conditions, the maximum equilibrium scour depth decreases by approximately 20%.

- (2) The scour protection ribs alter the characteristics of the scour flow field by impeding the downward movement of subsurface water flow along the structure. These vortices generate vortices near the scour protection ribs, dissipating energy from the surrounding water flow and reducing the intensity of subsurface flow and horseshoe vortices, thereby diminishing scour effects. The presence of scour protection ribs leads to a decrease in bed shear stress, and as the scour terrain develops, the reduction rate of bed shear stress gradually increases. Initially, the maximum bed shear stress reduction rate is approximately 8.3%, resulting in a similar development rate of the maximum scour depth in the early stages of the experiment. In the equilibrium scour terrain, where the scour pit no longer changes, the overall bed shear stress decreases, and the reduction rate with scour protection ribs is approximately 50.6%. Consequently, the late-stage development rate of the maximum scour depth is lower than that in the unprotected condition, indicating an enhanced protective effect.
- (3) Increasing the length of scour protection ribs enhances their protective effect on bed sediment. However, continuous lengthening does not result in a continuous increase in protection; therefore, an appropriate length of scour protection ribs should be chosen. The spacing between scour protection ribs influences their protective effect on bed sediment. A smaller spacing does not continuously enhance the protective effect; it may exacerbate scour due to excessive density, increasing the obstruction area and intensifying the scour. A greater spacing may diminish the protective effect of scour protection ribs. Therefore, selecting an appropriate spacing is crucial. The unique concave grooves in L-shaped scour protection ribs enhance their obstructive effect on subsurface water flow, reducing bed shear stress. Therefore, adopting more efficient scour protection rib shapes can enhance the protective effects of these materials.

It should be noted that conclusions about the design parameters of anti-scour ribs on local scour were drawn based on numerical simulations without experiments. The assessment of shear stress enables a rapid preliminary evaluation of the effectiveness of local scour protection measures. Subsequent experimental studies of the design parameters of anti-scour rib and more simulations including sediment model are required and useful for drawing a general and solid conclusion.

Acknowledgments

The authors would like to thank their colleagues from Southwest Jiaotong University for their assistance and discussions.

Authors' contributions

Conceptualization, PR; Formal analysis, PR and KW; Investigation, PR and BZ; Supervision, KW, YL; Writing—original draft, PR and KW; Writing—review and editing, PR, KW, BZ, LW, RN, YL. All the authors have read and agreed to the published version of the manuscript.

Funding

This work was supported financially by the National Natural Science Foundation of China (Grant Nos. U21A20154 and 52222804).

Availability of data and materials

All the data are presented in the published article.

Declarations**Competing interests**

The author(s) declare no potential conflicts of interest with respect to the research, authorship, and/or publication of this article.

Received: 24 January 2024 Accepted: 15 March 2024

Published online: 17 April 2024

References

- Abbas FM, Naeem UA, Ghani U, Khan A, Ahmad TF (2020) Experimental study of inclined bridge pier scouring. *Mehran Univ Res J Eng Technol* 39(4):859–870
- Abdelmoaty MS, Zayed M (2021) Using side flow jets as a scour countermeasure downstream of a sluice gate. *Beni-Suef Univ J Basic Appl Sci* 10(1):88
- Administration FH (2012) Evaluating Scour at Bridges (Fifth Edition). Hydraulic Engineering Circular No. 18. Publication No. FHWA-HIF-12-003 (Evaluating Scour at Bridges (Fifth edition). Hydraulic Engineering Circular No. 18. Publication No. FHWA-HIF-12-003)
- Ahamed A (1995) Visualization and Image Processing of Juncture Vortex System. *Proceeding of Isfv*
- Chiew Yee-Meng (1992) Scour protection at bridge piers. *J Hydraulic Eng* 118(9):1260–1269
- Chiew YM (1997) Mechanics of Riprap Failure at Bridge Piers. *J Hydraul Eng* 121(9):635–643
- Dargahi B (1989) The turbulent flow field around a circular cylinder. *Exp Fluids* 8(1):1–12
- Dargahi B (1990) Controlling Mechanism of Local Scouring. *J Hydraulic Eng* 116(10):1197–1214
- Smith DW (1977) Why Do Bridges Fail. *Civ Eng* 47(11):58–62.
- Guan D, Wang L, Ma L, Melville BW (2022) Fluctuating frequency of live bed scour depth around submerged weirs at equilibrium stages. *J Hydraulic Eng* 148(4):06022001
- Khaledi V, Amini A, Bahrami J (2020) Physical simulation of scour width and length variation around complex piers under clear water condition. *Marine Georesour Geotechnol* 39(9):1107–1114.
- Kumar V, Raju KGR, Vittal N (1999) Reduction of Local Scour around Bridge Piers Using Slots and Collars. *J Hydraul Eng* 125(12):1302–1305
- Kw An RTF, Melville BW (1994) Local scour and flow measurements at bridge abutments. *J Hydraulic Res* 32(5):661–673
- Lauchlan CS, Melville BW (2001) Riprap protection at bridge piers. *J Hydrol Eng* 127(5):412–418
- Lu X, Wei K, Deng K, Xu L (2024) Lifetime seismic resilience assessment of a sea-crossing cable-stayed bridge exposed to long-term scour and corrosion. *Ocean Eng* 295:116990
- Luo K, Si Y, Lu S, Liang B, Qi H (2022) Characteristics of reducing local scour around cylindrical pier using a horn-shaped collar. *J Eng Appl Sci* 69(1):105
- Melville BW, Hadfield AC (1999) Use of Sacrificial Piles as Pier Scour Countermeasures. *J Hydraul Eng* 125(11):1221–1224
- Melville BW (1975) Local scour at bridge sites. Dissertation, University of Auckland New Zealand
- Moncada-M AT, Aguirre-Pe J, Bolívar JC, Flores EJ (2009) Scour protection of circular bridge piers with collars and slots. *J Hydraul Res* 47(1):119–126
- Parola AC, Mahavadi SK, Brown BM, El Khoury A (1996) Effects of rectangular foundation geometry on local pier scour. *J Hydraul Eng* 122(1):35–40
- Qiu F, Wei K, Xiang Q, Jiang Z (2023) Effects of local scour and caisson geometry on the drag force of bridge foundations under steady flow. *Appl Ocean Res* 133:103506
- Raudkivi AJ, Ettema R (1983) Clear-water scour at cylindrical piers. *J Hydraul Eng* 109(3):338–350
- Roulund A, Sumer BM, Fredsoe J, Michelsen J (2005) Numerical and experimental investigation of flow and scour around a circular pile. *J Fluid Mechn* 534:351–401
- Soulsby R (1997) Dynamics of marine sands.
- Unger J, Hager WH (2007) Down-flow and horseshoe vortex characteristics of sediment embedded bridge piers. *Exp Fluids* 42(1):1–19
- Wang C, Yu X, Liang F (2017) A review of bridge scour: mechanism, estimation, monitoring and countermeasures. *Nat Hazards* 87(3):1–26
- Wang S, Wei K, Shen Z, Xiang Q (2019) Experimental investigation of local scour protection for cylindrical bridge piers using anti-scour collars. *Water* 11(7):1515
- Wei K, Zhong X, Cai H, Li X, Xiao H (2024) Dynamic response of a sea-crossing cable-stayed suspension bridge under simultaneous wind and wave loadings induced by a landfall typhoon. *Ocean Eng* 293:116659
- Wei K, Qiu F, Qin S (2022) Experimental and numerical investigation into effect of skirted caisson on local scour around the large-scale bridge foundation. *Ocean Eng* 250:111052
- Xiang Q, Wei K, Li Y, Zhang M, Qin S (2020) Experimental and Numerical Investigation of Local Scour for Suspended Square Caisson under Steady Flow. *KSCCE J Civ Eng* 24(9):2682–2693
- Zarrati AR, Gholami H, Mashahir MB (2004) Application of collar to control scouring around rectangular bridge piers. *J Hydraulic Res* 42(1):97–103

Publisher's Note

Springer Nature remains neutral with regard to jurisdictional claims in published maps and institutional affiliations.